

Interfacial energy constraints are sufficient to align cells over large distances

S. Tlili¹, M. Shagirov¹, S. Zhang¹ and T. E. Saunders^{1,2,3,#}

¹ Mechanobiology Institute, National University of Singapore, Singapore

² Department of Biological Sciences, National University of Singapore, Singapore

³ Institute of Molecular and Cell Biology, A*Star, Singapore

Correspondence: dbsste@nus.edu.sg

During development and wound healing, cells need to form long-ranged ordered structures to ensure precise formation of organs and repair damage. This requires cells to locate specific partner cells to which to adhere. How such cell matching reliably happens is an open problem, particularly in the presence of biological variability. Here, we use an equilibrium energy model to simulate how cell matching can occur with subcellular precision. A single parameter – encapsulating the competition between selective cell adhesion and cell elasticity – can reproduce experimental observations of cell alignment in the *Drosophila* embryonic heart. This demonstrates that adhesive differences between cells (in the case of the heart, mediated by filopodia interactions) are sufficient to drive cell matching without requiring cell rearrangements. The model can explain observed matching defects in mutant conditions and when there is significant biological variability. We also demonstrate that a dynamic vertex model gives results consistent with the equilibrium energy model. Overall, this work shows that equilibrium energy considerations are consistent with observed cell matching in cardioblasts, and has potential application to other systems, such as neuron connections and wound repair.

Introduction

During development, cells interact collectively to form tissues and organs through a series of morphological transformations, driven by cell proliferation, rearrangements, migration and death¹⁻⁴. When these processes fail, the final shape of the tissue can be defective, resulting in diseases, including cardiomyopathies⁵ and neurological defects^{6,7}. During organogenesis, cells often need to identify specific cells to which to adhere. A classic example is formation of human facial structures⁶; cells initially undergo long-ranged migration from distinct regions of the neural plate before forming precise connections to create structures such as the lip. Errors in this process lead to birth defects such as cleft lip and facial cleft⁷. During neurogenesis, neurons also need to form precise linkages to their synaptic partners⁸⁻¹⁰ with severe consequences if these processes fail. A range of molecules have been identified that are involved in cell matching, predominantly from neuronal systems¹¹⁻¹⁴. These molecules include cytoskeletal, adhesion, and force transducing proteins. However, the underlying mechanisms by which the information from these different components is integrated by the developing tissue to form precise connections remain unknown.

In most tissues, there are multiple cell types with stereotypic spatial positions. For example, formation of the eye requires precise cell fate determination and positioning^{15,16}, even within a growing domain¹⁷. In the developing heart, cardioblasts take on different fates depending on expression of (highly conserved) transcription factors¹⁸. Periodic patterns of cells can also be generated from lateral inhibition^{19,20}. Such periodic patterns need to be maintained across large distances, even as tissues undergo large-scale morphological changes.

Theoretical modelling of tissue formation has helped increase our understanding of how cells pack²¹, form compartment boundaries²², generate complex tissue shapes²³⁻²⁶, and ensure regulated growth²⁷. Lateral inhibition can create a wide variety of patterns depending on the feedback mechanisms²⁸. Recently, vertex models have been used to understand cell structure in epithelia^{29,30}. Although biological systems are inherently dynamic, equilibrium statistical mechanics can be a powerful tool for understanding suitable biological processes. An example of such a case is cell packing in the eye, where analogies with soap bubbles provide an effective tool for understanding formation of the *Drosophila* retina³¹.

Here, we develop a model of cell matching where differential adhesion energy constraints between cells drives the process of matching. We apply this to the developing *Drosophila* embryonic heart, where the process of cardioblast cell matching has recently been quantified³². The *Drosophila* embryonic heart is comprised of two lines of cardioblasts that migrate together over a period of a few hours, Figure 1A, and they express either Tinman (Tin, the *Drosophila* homolog of mammalian Nkx2.5) or Seven-up (Svp), Figure 1B, in a repeating 4-2 pattern³³. As cardioblasts approach each other, the cells adjust position, via filopodia interactions between cardioblasts, to align accurately with their contralateral partners, Figure 1C-D. Specific adhesion molecules are expressed within the different cardioblast types: Fasciclin III (Fas3) in Tin-positive cardioblasts; and Ten-m in Svp-positive cardioblasts, Figure 1E. Cell matching in the heart, as defined in Figure 2A, depends on the differential spatial expression of these adhesion molecules³², Figure 2B-C. Motivated by these observations, we construct a biophysical model of the cell-cell interactions to test whether such differential adhesion is sufficient to drive cell matching. We then use this model to test how both structural and genetic perturbations alter cell matching. This model provides a biophysical framework in which to understand how cells find specific partners during development.

Results

Mapping of adhesive interactions between filopodia onto an equilibrium energy state

To simulate cell matching, we developed an energy-based model that accounts for the spatial constraints between cells and the adhesion competition between different cell types. In the *Drosophila* heart, differential adhesion between cells is mediated by filopodia contacts, which have a spread of contact times³², from a few seconds to over five minutes. As justified below, the underlying principle of the model is that these differential filopodia adhesion times between adhering cells can be mapped onto effective adhesion energies.

At a biochemical level, the time for reactions, τ , are typically related to the Arrhenius law: $\tau \sim \tau_0 e^{\Delta E/k_B T}$, where ΔE is the energy cost of the reaction. It has recently been shown that time scales in biological systems at macroscopic levels can also follow the Arrhenius law, such as in the developmental time of *Drosophila* embryogenesis^{34,35}. Here, we apply a *mesoscopic* approximation, where we assume that the distribution of binding times of filopodia τ_{bind} can be related to the effective adhesion energy barrier ΔE_{adh} to separate contacting filopodia.

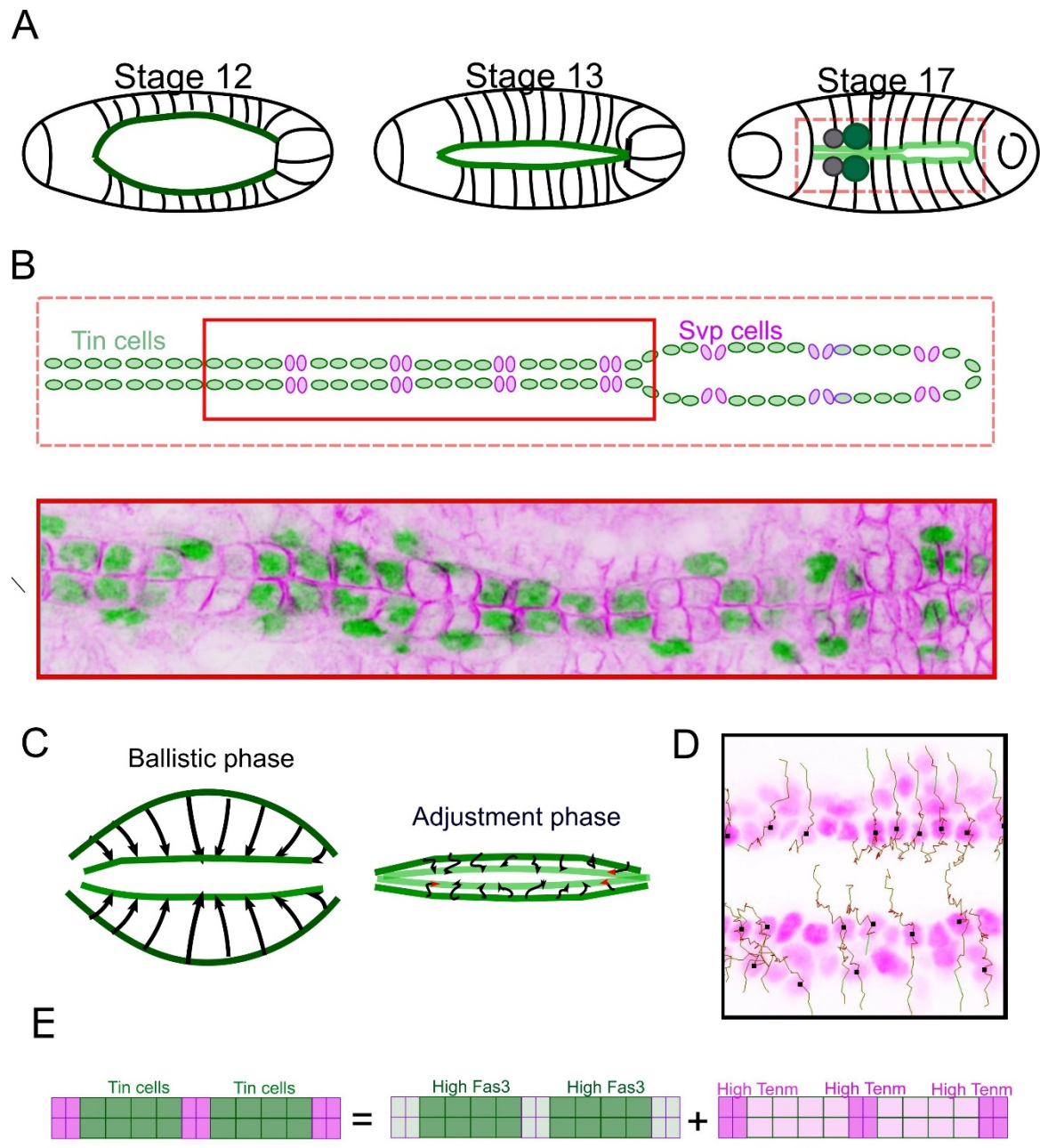


Figure 1. **Cell matching in *Drosophila* embryonic heart.** (A) Developmental stages of heart formation. Cardioblasts (green regions) merge to form a tubular heart. (B) Cardioblasts have distinct expression patterns. Heart structure at larval stage: the heart is made of a periodic alternation of Tin cells and Svp cells. Staining of cardioblasts (Spectrin in magenta and Tinman in green). (C) Heart formation is initially driven by global tissue movement during dorsal closure but active processes align cells in a final adjustment phase. (D) Example of cell trajectories during the adjustment phase. (E) Cardioblasts express the adhesion molecules Fas3 and Ten-m in an alternating pattern.

In the model, the overlap between facing cells results in an adhesion energy $\Delta E = -\epsilon \cdot x$, where x denotes the length of the cell contact interface and ϵ is the adhesion energy per unit length between the two cells, Figure 2D. Cellular compressibility for each cell is encoded by an effective elastic energy $E_{el} = K(L_{cell} - L_0)^2$, corresponding to the cost of deforming the cells away from their preferred cross-sectional width; K is the effective cell compressibility along its leading edge, L_{cell} the cell length and L_0 the cell rest length, Figure 2D. We only focus on the apical leading edge of the cells as this is where the process of cell alignment is occurring. Combining the energy scales, we can express effective energies for two cell types, denoted by a and b :

$$E_a = K(L_{cell} - L_{0,a})^2 - (\epsilon_{aa} \cdot x + \epsilon_{ab} \cdot y) \quad (1)$$

$$E_b = K(L_{cell} - L_{0,b})^2 - (\epsilon_{bb} \cdot x + \epsilon_{ab} \cdot y) \quad (2)$$

ϵ_{ab} denotes the adhesion energy per unit length between cells of type a and b , x and y denote the total alignment overlap with cells of the same and different types respectively, and $L_{0,a}$ and $L_{0,b}$ represent the equilibrium lengths for the different cell types.

Filopodia activity results from the interplay between active fluctuations and adhesion interactions with other filopodia. The active alignment of the heart takes place over a period of around 30 minutes, whereas the average binding time of filopodia is 1-5 minutes. In the following, we assume that the heart has enough time during the active alignment process to reach equilibrium.

To simulate the evolution and equilibration of configurations of heart cell, we use a Metropolis algorithm incorporating mechanical fluctuations induced by filopodia activity as an effective temperature, see Figure 2E and Methods for further details. We define cellular mismatch by identifying the fraction of cell boundaries that are not correctly aligned with their corresponding opposite cell, Figure 2A. In this definition, a perfectly aligned tissue has mismatch of 0, while a fully misaligned system has a mismatch of 1. The tissue mismatch is then taken as the average over all cell mismatches.

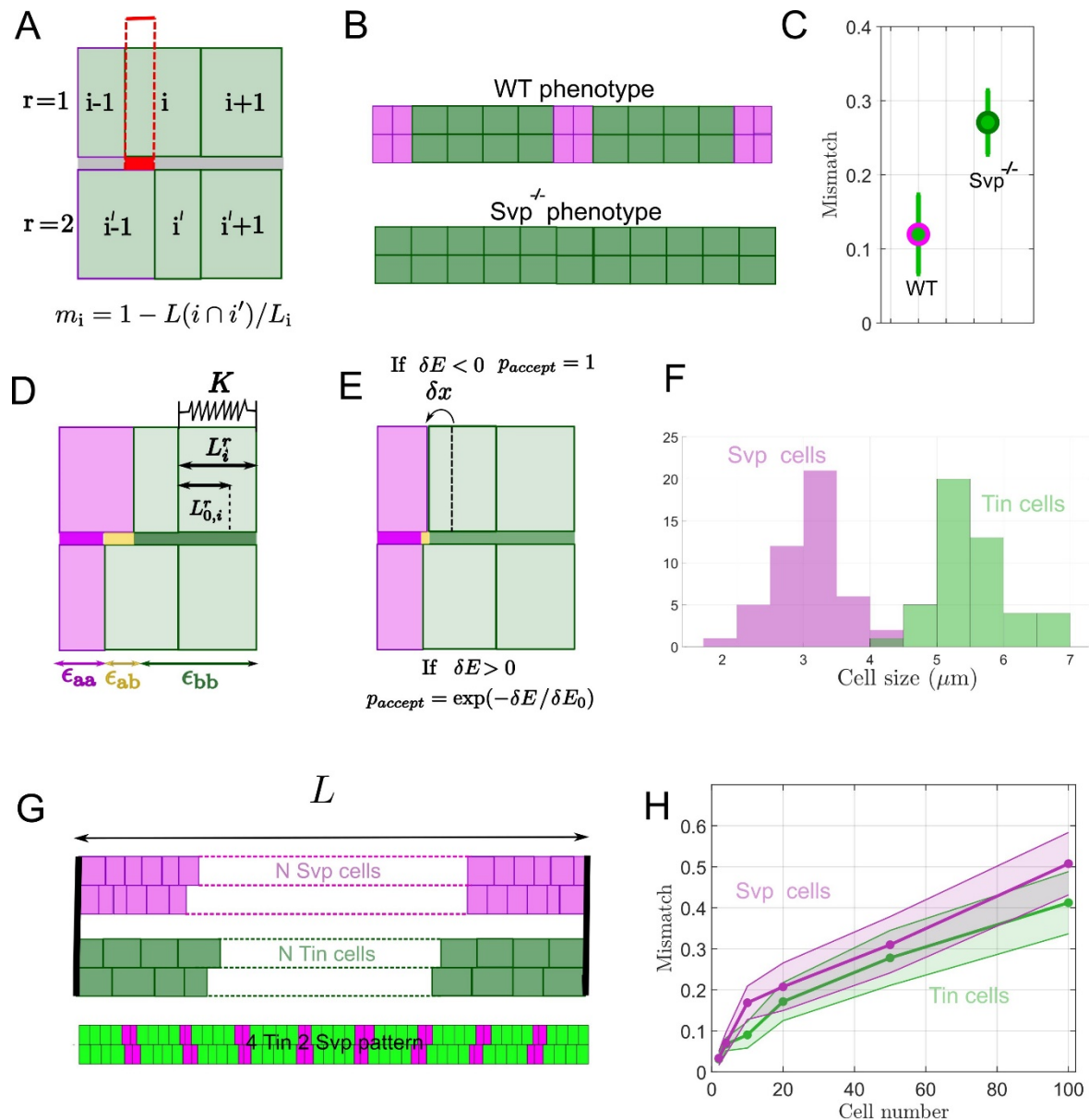


Figure 2: Simulating heart matching (A) Definition of cell mismatch. $r=1,2$ denotes two contralateral rows of cardioblasts. (B,C) When different cell types are not present (as in $svp^{-/-}$), the resulting heart has severe mismatching defects. (D) Cells can deform elastically from their rest length with a compressibility K and cell-cell contact is characterized by an adhesion depending of the contact type. (E) Metropolis algorithm is used to find the final cell alignment after equilibration. At each step, a cell/cell interface is randomly chosen and is displaced by δx , which follows a Gaussian distribution (see Methods). The probability to accept the displacement follows the Metropolis algorithm (F) Distribution of leading edge size in different cardioblast types. (G) Simulations with only one cell type (all Svp or all Tin) and with the alternated pattern of Tin/ Svp cells. (H) Predicted mismatch in hearts with one cell type for different cells number.

Minimization of interfacial energy constraints are sufficient to explain cell alignment in the wildtype *Drosophila* heart

We apply our model to the developing *Drosophila* heart, where quantitative data for cell matching is available³². As well as incorporating the effective energy differences, we need to implement within the simulation a representative pattern of cell types. In the *Drosophila* heart, Tin-positive cardioblasts express Fas3 at high levels and Svp-positive cardioblasts express Ten-m. We translate this into different adhesion energies per unit length between Tin-positive cardioblasts (ϵ_{TT}), Svp-positive cardioblasts (ϵ_{SS}), and between Tin- and Svp-positive cardioblasts (ϵ_{ST}), similar to the outline given in Figure 1B-E.

Initial configuration of the cells and initial cell alignment: By the end of dorsal closure, cardioblasts are brought into close contact. To initiate the cellular arrangement, we assume that the cells at the two ends of the heart are perfectly aligned and are at their resting length initially. To model geometric disorder, we take the length of the apical surfaces for Tin-positive and Svp-positive cardioblasts as $L_{0,T}$ and $L_{0,S}$ respectively. These lengths are simulated as Gaussian variables of mean $L_{0,T}^{mean}$ and $L_{0,S}^{mean}$ with standard deviation $L_{0,T}^{std}$ and $L_{0,S}^{std}$, extracted from experimental quantification of cell size (Figure 2F). We construct the simulated heart as two rows of cells formed by a succession of four Tin-positive cells and two Svp-positive cells patterns, with a total number of $N_1 = 52$ cells (number of cells in a heart row, Figure 1B and 2G). Each cell length is picked as a random variable according to the rest lengths distributions (Figure 2F). However, we constrain the total lengths of the two rows to be identical (Methods).

Initial cell matching without adhesion energy: We first consider the question: are the boundary constraints alone sufficient to ensure robust cell matching? To answer this, we take initial conditions that mirror experimentally measured cardioblast size and position (Figure 2F-G) but with no adhesion energy (*i.e.* $\epsilon_{TT} = \epsilon_{SS} = \epsilon_{ST} = 0$), Figure 2D. As we take cells at their initial rest length, no equilibration is needed and we calculate the mismatch of the initial condition. We simulate $N_2 = 30$ embryos with confinement of different sizes, and calculate the ensemble mismatch in cell alignment. This results in a mismatch increasing with system size, Figure 2H. Interestingly, we find for $N_1 = 52$ cells (the experimental size of the heart) a mismatch around 0.3 which corresponds to the mismatch value experimentally observed in the *Svp*^{-/-} mutants where all cells are of the same type, Figure 2C. In summary, geometric disorder, induced by cell size variability, is too large to enable precise cell matching merely by boundary constraints.

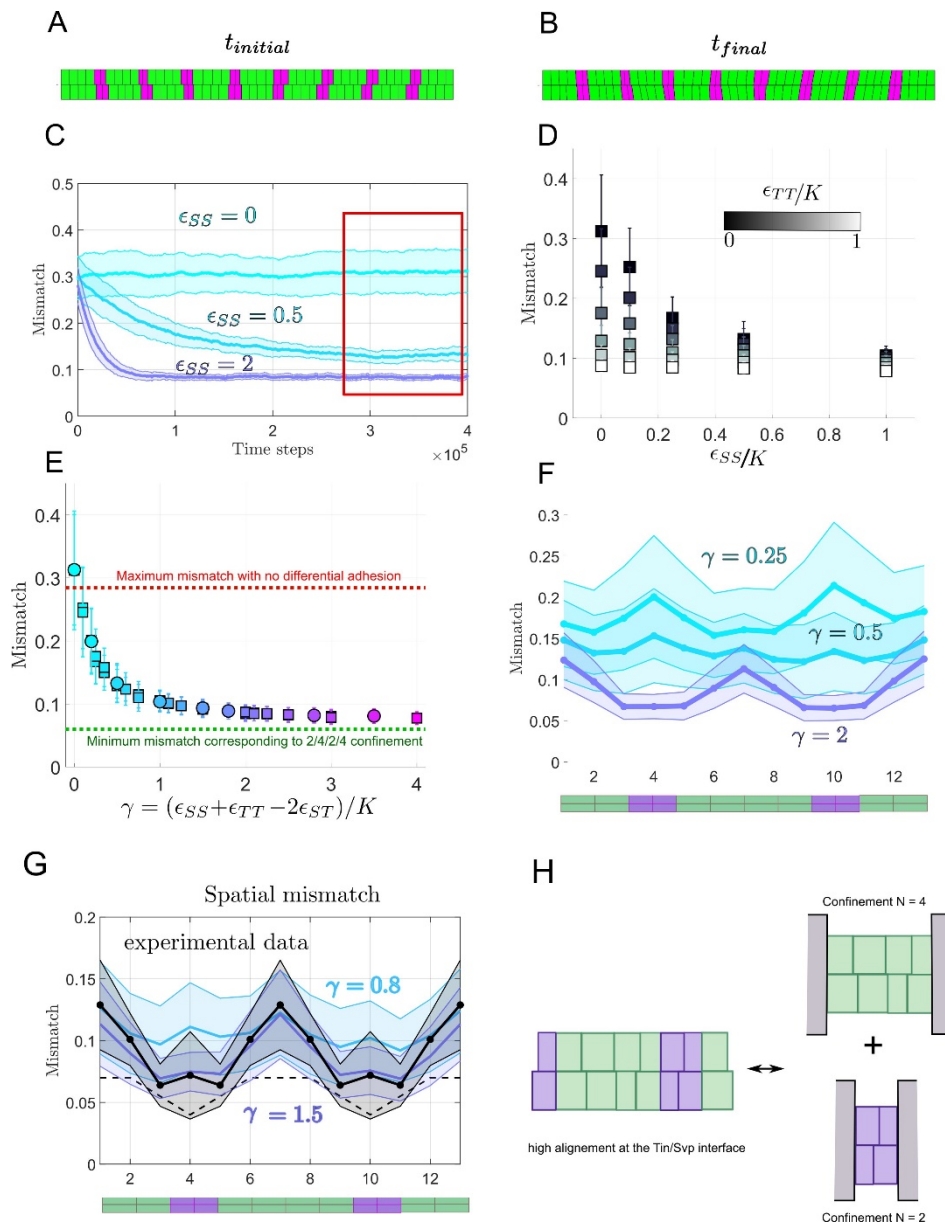


Figure 3: The interplay between differential adhesion, cell compressibility and cell size variability determines the cell-matching. (A) Initial configuration randomly sampled for 52 cells (4 Tin/2 Svp alternated pattern). (B) Cells configuration after convergence of mismatch, cell lengths have changed on the cell/cell interface while we still represent their initial length and position on the side not touching the interface. (C) Ensemble averaged ($N_2 = 30$ simulated embryos) mismatch evolution for different values of ϵ_{SS} and $K = 1$. All mismatches are calculated at steady state. (D) Final mismatch for different values of ϵ_{SS} and ϵ_{TT} . (E) Final mismatch for different values of γ . Circles correspond to the case $\epsilon_{ST} = 0$ and squares to $\epsilon_{ST} \neq 0$. (F) Spatial variation of mismatch across different cell types as depicted in the below cartoon (green = Tin positive cardioblasts, magenta = Svp positive cardioblasts). (G) Spatial variations of the mismatch in the wildtype (in black) and comparison with the simulation (blue, purple). (H) Sketch showing how differential adhesion aligns heterogeneous cell-cell contacts, which generates local confinement of cells.

Calculating the mismatch with differential cell adhesion: We next investigate how the strength of selective adhesion impacts alignment. We first explore matching variations with only one cell type adhering, *i.e.* we vary ϵ_{SS} alone with $\epsilon_{TT} = 0$ $\epsilon_{ST} = 0$, Figure 3A-C. We compute mismatch evolution of the embryo as a function of simulation iterations and take its value once it reaches a steady-state value, Figure 3C. The final mismatch for a single embryo simulation is averaged over 30 embryos. We find that the final mismatch decreases with increasing adhesion level. We then explored two cell types with selective adhesion by using different combinations of ϵ_{SS} and ϵ_{TT} with $\epsilon_{ST} = 0$, Figure 3D. Different combinations of ϵ_{SS} and ϵ_{TT} can lead to the same alignment. By systematically varying ϵ_{SS} , ϵ_{TT} and ϵ_{ST} , we see that the equilibrium mismatch is determined by the parameter $\gamma = \frac{(\epsilon_{TT}-\epsilon_{ST})+(\epsilon_{SS}-\epsilon_{ST})}{K}$, representing the competition between cells due to differential adhesion and cell compressibility, Figure 3E. Here, γ corresponds to the typical length change that adhesion differences can generate for a single cell. For $\gamma = 0\mu m$, there is no energy cost for different cell types to have a contact interface. The mismatch corresponds to the random case simulated in Figure 2H; similar to the *Svp*^{-/-} mutant, where all cells are of the same type. Mismatch decreases with increasing γ , reaching a plateau around mismatch of ~ 0.07 , dashed line in Figure 3E. This implies that, beyond a certain level, increasing differential adhesion only weakly improves matching.

We measure spatial variations of the mismatch, denoted by m , Figure 3F. We find that m is minimal at the Tin-Svp interface, as any contact between different cell types has some adhesion energy cost for $\gamma > 0\mu m$, Figure 3G. Alignment of cells inside a block of homogeneous cell types in the high γ limit is determined by the boundaries imposed by the highly aligned cells at the interface between different cell types. Within a region of Tin-positive cells, the level of cell mismatch converges towards the non-adhesive random case with $N = 4$, Figure 3H. The mismatch between Svp-positive cells is similar to the random adhesion case with $N = 2$. The geometric variability in the lengths of the cell leading edges means that cells never reach zero mismatch even at very high adhesion values. Interestingly, for small values of γ , the pattern of cell mismatch is inverted, as geometric variability is higher for Svp cells.

Comparing the spatial profile of cell matching to the experimental data, we see that for $\gamma > 1\mu m$ the mismatch profile agrees well with experiment, Figure 3G. Therefore, simple energy considerations, with a single fitting parameter γ , are sufficient to reproduce the wildtype matching phenotype.

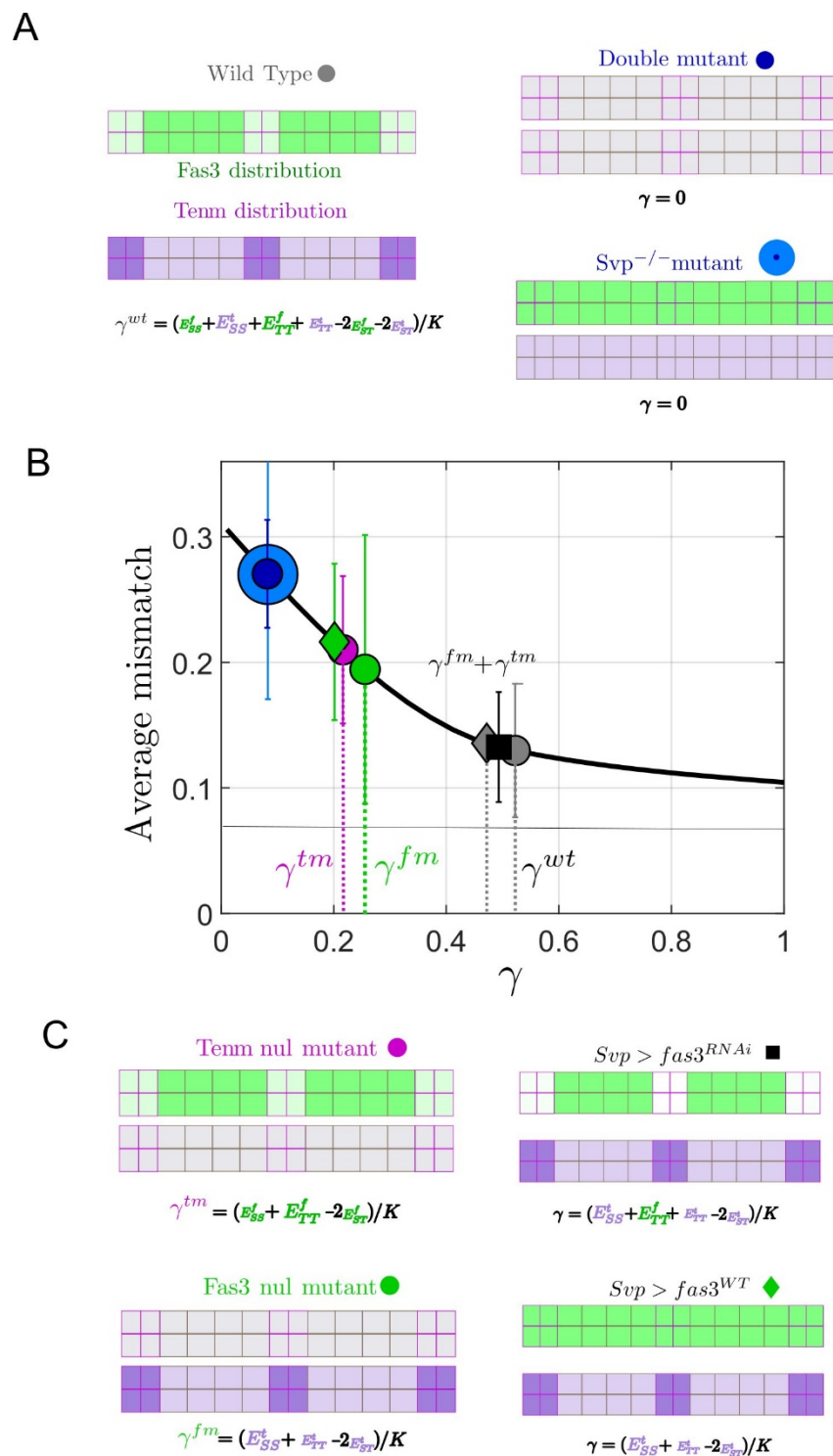


Figure 4: **Equilibrium energy description replicates experimental observations in wild type and mutants.**

(A,B,C) Distribution of Fas3 (green) and Ten-m (purple) in wildtype and mutant embryos. The value of γ for wild type (grey circle), double mutant (blue small circle), *svp*^{-/-} mutant (blue circle), *fas3*^{-/-} (green circle), *ten-m*^{-/-} (purple circle), Svp-Gal4, Fas3-UAS (green diamond) and Svp-Gal4 > Fas3-RNAi-UAS (black square) embryos can be inferred from the average mismatch curve.

Energy scales are just sufficient to ensure robust matching

Perturbing the expression profiles of Fas3 and Ten-m, results in altering of the cardioblast cell matching³². We next ask whether the model can reproduce these observations. To that end, we use Figure 3E to estimate γ for wild type and mutants conditions (Figure 4A-C) given the experimentally measured cell mismatch. We do not know the specific effective energy levels associated with different adhesion interactions. To relate the values of ϵ_{TT} , ϵ_{SS} and ϵ_{ST} to the underlying dynamics, we assume that they depend on the energy scales of homophilic interactions of Fas3 (ϵ_{aa}^{Fas3}) and Ten-m (ϵ_{aa}^{Ten}), e.g. $\epsilon_{TT} \approx \epsilon_{TT}^{Fas3} + \epsilon_{TT}^{Ten}$.

Our model predicts that mutants erasing the differential pattern of expression of Fas3 and Ten-m lead to $\gamma = 0 \mu m$ and a mismatch equal to the random case. This is the case for the double mutant of *Fas3*^{-/-} and *Ten-m*^{-/-} and the mutant *svp*^{-/-} (Figure 4A,B). For the wild type, we find $\gamma_{WT} \sim 0.5 \mu m$ which is smaller than the value $\gamma_{WT} \sim 1 \mu m$ found by fitting the experimentally measured spatial variation of mismatch (Figure 3G). However, this difference could be explained by the shallowness of the mismatch curve for $\gamma > 0.5 \mu m$. Assuming that there is no interaction between Fas3 and Ten-m, we expect that $\gamma_{WT} = \gamma_{Fas3} + \gamma_{Tenm}$. Using the measured matching in mutants of Fas3 *Fas3*^{-/-} and Ten-m *Ten-m*^{-/-}, we estimate the contributions to γ_{WT} from the different adhesion molecules, and find $\gamma_{Fas3} + \gamma_{Tenm} \sim \gamma_{WT} \sim 0.5 \mu m$ (Figure 4B).

Our simple additive model of energies is consistent with other mutant observations. When Fas3 is overexpressed in Svp cells using Svp-Gal4, Fas3-UAS expressing embryos, we expect γ to be the same than for the mutant *Fas3*^{-/-}, which is the case (Figure 4B-C). When the level of Fas3 in Svp-positive cells is reduced using embryos expressing Svp-Gal4 > Fas3-RNAi-UAS, ϵ_{SS} is reduced compared to wildtype, but so is ϵ_{ST} as direct interactions between filopodia with Fas3 is reduced between different cell types. We find a γ similar to the wild-type case showing that ϵ_{ST} is small compared to ϵ_{SS} and ϵ_{TT} .

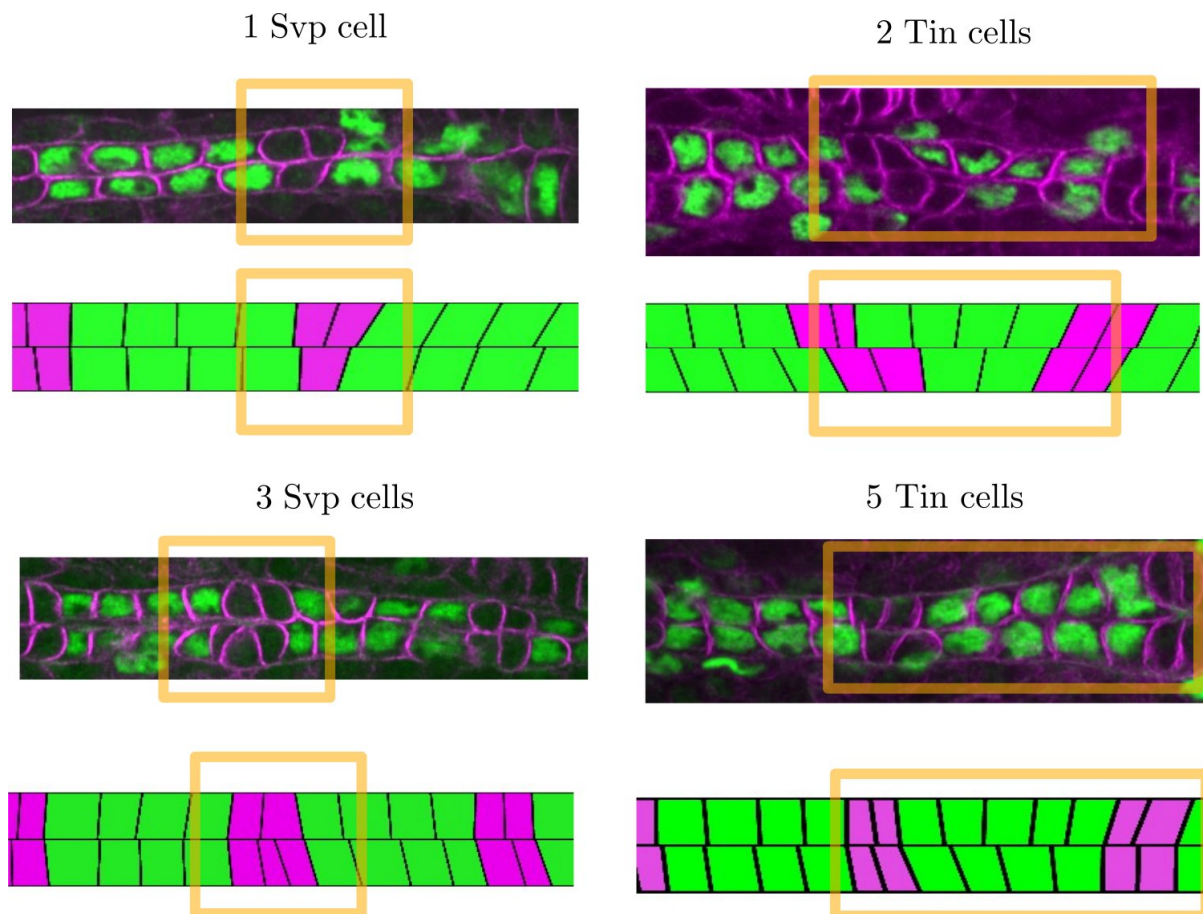


Figure 5: **Matching correction of local defects.** Various types of experimentally observed cell number defects in wild type embryonic hearts. Differential adhesion can partially compensate these defects by deforming cells in the range of $\gamma \approx 0.5$ found in Fig.4.

Robustness of cell matching to perturbations

Here, we probe the robustness of the system to perturbations in cell number by considering variations in cell type specification. Within wildtype embryo populations, we observe variability in the spatial pattern of cardioblast specification. For example, we have observed embryos with three and five Tin-positive cardioblasts in a sector, as well as a solitary Svp-positive cardioblast, and an additional one (Figure 5). Even when cell number is perturbed, we observe that the boundaries between different cell types are typically well defined. To test the model, we implemented different initial patterns of cardioblasts but otherwise kept parameters identical to the wildtype scenario with $\gamma = 0.5 \mu m$. The system equilibrates to a state with clear boundaries between the different cell types and cells deform to align boundaries. This demonstrates that having two complementary adhesion processes is robust to perturbations in the structure of the heart as it develops.

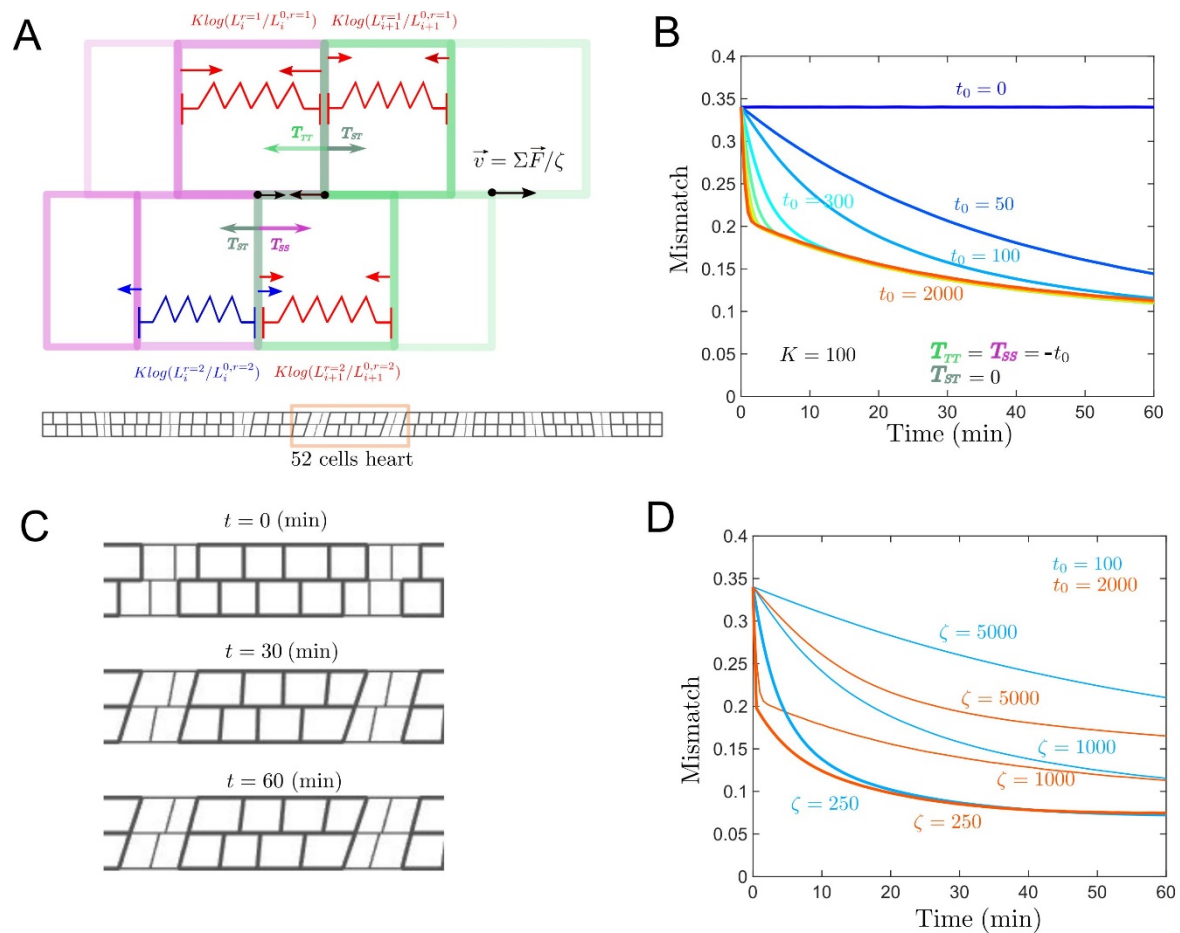


Figure 6: Simulating cell matching dynamics (A) Vertex model implementation of interface dynamics. Each cell-cell lateral boundary on a row is defined by a vertex point. Elastic forces are represented in red/blue depending if cells are stretched/compressed. Each cell-cell interface section between the two facing rows has a negative tension which acts on the vertices applying forces represented in magenta/green/grey depending on the interface type. The sum of these contributions divided by a friction coefficient, ζ , gives the vertex velocity. (B) We evolve the system (Methods) and compute the ensemble averaged mismatch over time ($N = 30$). We vary the tension t_0 between 0 and 2000 while K is fixed to 100 and $\zeta = 1000$. (C) Spatial alignment for 0 min, 30 min, 60 min for $t_0 = 2000$, $K = 100$ and $\zeta = 1000$ (D) Adhesion-independent cell alignment between cells of the same type depends on the friction coefficient ζ . Results shown for two different tensions, t_0 .

Dynamic vertex model of cell matching

To evaluate how differential adhesion modulates cell matching dynamics, we used a vertex approach to model the time evolution of vertices at the interface between the two facing rows of cells, Figure 6A (see Methods). By analogy with the equilibrium energy model used previously, vertices are submitted to elastic forces corresponding to effective elasticity and

adhesion forces in the cell. We assume that adhesion produces a negative tension, which extends cell-cell contact interfaces. The sum of these contributions results in a force which, when divided by an effective friction coefficient, gives the vertex velocity. We explore the simple case of equal tensions, $T_{SS} = T_{TT} = -t_0$ and $T_{ST} = 0$ with a fixed K and friction coefficient, ξ . Varying t_0 , keeping other parameters fixed, shows a lower limit to cell matching accuracy, as the time evolution of cell matching collapses onto a single curve for large t_0 , Figure 6B. This limit is consistent with our equilibrium model. At high adhesion differences, the cell mismatch first undergoes a rapid decrease, which is adhesion-dependent. This corresponds to the phase of heterogeneous cell types boundaries shrinking. Below a mismatch of ~ 0.2 , the boundaries between cell types are perfectly aligned, Figure 6C. The mismatch between cells of the same type decreases with slower, adhesion independent, dynamics that are friction dependent, Figure 6D. Overall, we see that dynamically incorporating differential adhesion gives similar results to our equilibrium approach, supporting our above assumptions.

Discussion

Even though biological systems are inherently out-of-equilibrium, we have demonstrated that an equilibrium energy argument is consistent with experimental observation of cell matching in the heart. This is consistent with the rapid dynamics of filopodia compared to the time of heart cells final alignment. The filopodia dynamics relate to the system effective temperature. The idea of effective temperatures in developing systems has also recently been used to describe jamming transitions during zebrafish development³⁶. Our model shows that cell matching results from the interplay between cell-cell interactions (mediated by filopodia and specific adhesion molecules) and cell deformability. According to our model, the level of differential adhesion found in the wildtype heart is close to the minimal level required to obtain a well-aligned heart as the value $\gamma = 0.5$ corresponds to the point where the mismatch curve in function of γ starts to flatten. We find that Fas3 and Ten-m contribute almost equally to the matching process. Furthermore, we demonstrate that increasing differential adhesion indefinitely does not accelerate the matching process beyond a certain point as the final alignment phase is adhesion independent.

A key result of our model is that short-ranged constraints (*i.e.* adhesion differences between two cell types) can propagate long-ranged order. We show that generating periodic segments

of different adhesion molecules (i) aligns these segments at their interfaces and (ii) alignment inside each segment is due to geometric confinement and decreases with the segment size.

Our work has potential application to other biological systems. During neurogenesis - where precise connections between neurons are required - Notch signalling (involve in lateral inhibition) has recently been shown to regulate neuronal wiring¹⁰. Formation of the vasculature requires cell migration to precise locations and this is mediated by filopodia protrusions and lateral inhibition³⁷. During wound healing, cells need to repair wounds by forming precise connections. However, how processes at a single cell level are integrated to ensure long-ranged precise cell matching remains an open question³⁸. In our model, we do not consider heterogeneities in the mechanical properties. In other systems such as the brain, tuning of tissue stiffness ensures precise cell matching³⁹. More generally, coordinated cell migration can be directed by tissue stiffening⁴⁰. It would be possible to test the role of mechanical feedback in our model by adding viscoelastic relaxation of the cell lengths within a vertex model framework as described in Figure 6.

Author Contributions

S.T. and T.E.S. designed the project with input from S.Z. S.T. and M.S. performed the simulations and modelling. S.Z. provided all experimental data. S.T. and T.E.S. wrote the manuscript, with contributions from M.S. and S.Z..

Acknowledgements

This work was supported by a Singapore Ministry of Education Academic Research Fund Tier 2 grant (MOE2018-T2-2-135), a Singapore National Research Foundation Fellowship (NRF2012NRF-NRFF001-094) and HFSP Young Investigator Grant (RGY0083/2016), all awarded to TES. Tinman antibody was a gift from Manfred Frasch.

Methods

Experiments

Experimental data collected as described in Zhang *et al.* ³².

Modelling

One-dimensional interface, and mismatch ratio definitions

The model system consists of two rows of equal number of cells interacting on a one-dimensional interface defined as vertices x . Each cell i on a row r is represented by a pair of vertices $(x_i^{(r)}, x_{i+1}^{(r)})$ on this interface with $x_i^{(r)} \leq x_{i+1}^{(r)}$ ($i = 1, 2, \dots, N + 1$, and $r \in \{1, 2\}$ for N cells occupying each row), with cell length

$$L_i^{(r)} = x_{i+1}^{(r)} - x_i^{(r)}. \quad (\text{SE1})$$

The total length of a model system is kept constant by fixing first $x_1^{(1)} = x_1^{(2)}$, and last $x_{N+1}^{(1)} = x_{N+1}^{(2)}$ vertices throughout the simulation. The overlap interval length between cells i and j located on two different rows is calculated as:

$$L(i \cap j) = \begin{cases} 0, & \text{if } \max(x_i^{(1)}, x_j^{(2)}) > \min(x_{i+1}^{(1)}, x_{j+1}^{(2)}) \\ \min(x_{i+1}^{(1)}, x_{j+1}^{(2)}) - \max(x_i^{(1)}, x_j^{(2)}), & \text{otherwise.} \end{cases} \quad (\text{SE2})$$

The mismatch ratio $m_i^{(r)}$ of a cell i on a row r is defined as a proportion of length of overlap with cells other than its sister cell i' , and the total cell length of i :

$$m_i^{(r)} = \frac{L_i^{(r)} - L(i \cap i')}{L_i^{(r)}}; \quad m_i^{(r)} \in [0, 1], \quad (\text{SE3})$$

where the sister cell is defined as a cell i' with same index as i but located on a different row (i.e. $i' = i$), an average mismatch ratio of two sister cells is then calculated as $(m_i^{(1)} + m_{i'}^{(2)})/2$.

Calculating net change in energy

All vertices $x_i^{(r)}$ are assumed to be coupled with harmonic springs, with each cell having an elastic energy $E_{\text{el},i}^{(r)} = K \cdot (L_i^{(r)} - L_{0,i}^{(r)})^2$, where $L_{0,i}^{(r)}$ is the equilibrium length for a given cell (kept constant throughout the simulation), and K is a spring constant. Then, the total elastic energy for the whole system is just a sum of elastic energies over all cells:

$$E_{el,total} = \sum_{r=1}^2 \sum_{i=1}^N K \cdot (L_i^{(r)} - L_{0,i}^{(r)})^2. \quad (SE4)$$

In the model, two rows of cells interact along the one-dimensional interface by adhesion of cells along segments of the interface shared by the same cell type cells, or by cohesion of cells of two different cell types along interface segments occupied by cells of two different types. We implemented the interface by defining interface vertices $x_j^{(int)}$ with $x_j^{(int)} \leq x_{j+1}^{(int)}$, which could be obtained by concatenating both rows of $x_i^{(r)}$ vertices into single vector and then sorting them. Similar to cell vertices ($x_i^{(r)}$), pair of interface vertices ($x_j^{(int)}, x_{j+1}^{(int)}$) represents an interface segment j . The total adhesion energy for the whole system is then the sum of adhesion energy contributions of all interface segments:

$$E_{adh,total} = \sum_{j=1}^{2N+1} \epsilon_j \cdot (x_{j+1}^{(int)} - x_j^{(int)}), \quad (SE5)$$

where ϵ_j is the cell type specific adhesion energy-per-unit length of a segment j :

$$\epsilon_j = \begin{cases} \epsilon_{aa}, & j \text{ is interface between type } a \text{ and } a \\ \epsilon_{bb}, & j \text{ is interface between type } b \text{ and } b \\ \epsilon_{ab}, & j \text{ is interface between type } a \text{ and } b \end{cases} \quad (SE6)$$

Since vertices of $x_j^{(int)}$ are from both rows of cells, changing position of a single cell vertex $x_i^{(r)}$ could result in cases with $x_j^{(int)} \geq x_{j+1}^{(int)}$, thus $x_j^{(int)}$ needs to be sorted before calculating total adhesion energy during simulation.

The total energy of the system as a function of location of cell vertices $x_i^{(r)}$ is calculated as the sum of elastic and adhesive energies:

$$E(x) = E_{el,total} + E_{adh,total} \quad (SE7)$$

and the nett change in total energy due to change in the configuration of $x \rightarrow x + \Delta x$ is calculated as a difference in total energy between the two configurations

$$\Delta E_{x \rightarrow x + \Delta x} = E(x + \Delta x) - E(x) \quad (SE8)$$

399

400 ***Sampling initial configuration and equilibrium lengths of cells***

401 Randomness in cell shape geometry was modelled as a random initial configuration of cells,
402 which was set to be equal to the equilibrium lengths of the cells throughout the simulation. The
403 random initial configuration of cells, and thus the equilibrium lengths ($L_{0,i}^{(r)}$) for each cell were
404 sampled from a normal distribution with cell type specific mean and standard deviation using
405 a MATLAB function *normrnd*. In order to construct a random configuration, we implemented
406 random sequential deposition⁴¹ of two rows onto each other with a constraint that enforces

equal length of two rows within $\varepsilon = \mu \cdot 10^{-3}$, where μ is the smallest of the two type-specific average lengths of the cells in the given configuration.

For the row of cells with m_a type a cells and $N - m_a$ type b cells, m_a equilibrium lengths ($L_{0,i}^{(1)}$) for the top row are sampled from a normal distribution with mean $L_{0,a}^{mean}$ and standard deviation $L_{0,a}^{std}$, and $N - m_a$ equilibrium lengths ($L_{0,i}^{(1)}$) are sampled from normal distribution with mean $L_{0,b}^{mean}$ and standard deviation $L_{0,b}^{std}$.

$$L_{0,i}^{(1)} \sim \begin{cases} \mathcal{N}(\mu = L_{0,a}^{mean}, \sigma = L_{0,a}^{std}) & \text{for type a} \\ \mathcal{N}(\mu = L_{0,b}^{mean}, \sigma = L_{0,b}^{std}) & \text{for type b} \end{cases}$$

where the mean and standard deviation for different cell types are experimentally determined parameters. Next, the bottom row equilibrium lengths ($L_{0,i}^{(2)}$) were sampled in the same manner until the constraint $\sum_i L_{0,i}^{(1)} - \varepsilon < \sum_i L_{0,i}^{(2)} < \sum_i L_{0,i}^{(1)} + \varepsilon$ was satisfied. Afterwards, $L_{0,i}^{(r)}$ are converted into cell vertices $x_i^{(r)}$ in the same sequence as the $L_{0,i}^{(r)}$ was produced by *normrnd* function.

Implementation of Markov-chain cell configuration sampling using Metropolis algorithm

In order to simulate evolution of the cell boundaries by moving cell vertices x and sample cell configurations, we used Monte Carlo Markov-chain (MCMC) sampling by implementing Metropolis algorithm in MATLAB⁴². At each MCMC sampling step a vertex $x_i^{(r)}$ is selected randomly and a random move is proposed $x_i^{(r)} \rightarrow x_i^{(r)} + \Delta x_i^{(r)}$, $\Delta x_i^{(r)}$ is a Gaussian random variable with mean 0 and standard deviation δX , the value of δX determines magnitude of the random movement (interpreted as random fluctuations in the model). In our implementation $\Delta x_i^{(r)}$ was sampled using *normrnd*(0, δX) function in MATLAB. Afterwards, Metropolis probability of accepting the proposed move, $p(x_i^{(r)} \rightarrow x_i^{(r)} + \Delta x_i^{(r)})$ is calculated using

$$p(x_i^{(r)} \rightarrow x_i^{(r)} + \Delta x_i^{(r)}) = \min \left(1, \exp \left(- \frac{\Delta E_{x_i^{(r)} \rightarrow x_i^{(r)} + \Delta x_i^{(r)}}}{E_0} \right) \right) \quad (\text{SE9})$$

where $\Delta E_{x_i^{(r)} \rightarrow x_i^{(r)} + \Delta x_i^{(r)}}$ is a nett change in total energy of the system due to movement of vertex $x_i^{(r)}$ by amount $\Delta x_i^{(r)}$, and E_0 is the effective temperature (“thermal energy”) of the cells. Then, $p(x_i^{(r)} \rightarrow x_i^{(r)} + \Delta x_i^{(r)})$ is compared to a uniformly distributed random variable δ_p in the

interval $\delta_p \in (0,1)$ produced by *rand* function in MATLAB. If the statement $\delta_p < p(x_i^{(r)} \rightarrow x_i^{(r)} + \Delta x_i^{(r)})$ is true, then the move is accepted, and otherwise the move is rejected.

Overall, the probability of movement $x_i^{(r)} \rightarrow x_i^{(r)} + \Delta x_i^{(r)}$ of a vertex at position $x_i^{(r)}$ is:

$$P(x_i^{(r)} \rightarrow x_i^{(r)} + \Delta x_i^{(r)}) = \frac{1}{2 \cdot (N - 1)} \cdot p(x_i^{(r)} \rightarrow x_i^{(r)} + \Delta x_i^{(r)})$$

where the first term on the right-hand-side refers to the probability of selecting vertex $x_i^{(r)}$ from two rows, and $N - 1$ vertices in each row (two end vertices on each row are assumed to be fixed throughout the simulation, and have $P = 0$). In order to avoid flipping of cells, and overlapping of cells on a single row, we forbid such movements by setting $p(x_i^{(r)} \rightarrow x_i^{(r)} + \Delta x_i^{(r)}) = 0$ for movements with $\Delta x_i^{(r)} > 0$ that exceed cell length of cell i (i.e. $\Delta x_i^{(r)} > 0$ AND $\Delta x_i^{(r)} > L_i^{(r)}$), and for movements with $\Delta x_i^{(r)} < 0$ that exceed cell length of cell $i - 1$ (i.e. $\Delta x_i^{(r)} < 0$ AND $|\Delta x_i^{(r)}| > L_{i-1}^{(r)}$).

Implementation of vertex model

Cell initial geometries are constructed using the same functions as with the equilibrium energy model above. Each vertex is described by its position $x_i^{(r)}(t)$, and follows the equation :

$\xi \frac{\partial x_i^{(r)}(t)}{\partial t} = (T_{adh}^{i+1} - T_{adh}^i + K \cdot \log(L_{i+1}^{(r)}(t)/L_{i+1,0}^{(r)}) - K \cdot \log(L_i^{(r)}(t)/L_{i,0}^{(r)})$ with $T_{adh} = T_{SS}$ for a S-S interface, $T_{adh} = T_{TT}$ for a T-T interface, and $T_{adh} = T_{ST}$ for a S-T interface. Here we use the elastic force form $K \cdot \log(L_i^{(r)}(t)/L_{i,0}^{(r)})$ instead of $K \cdot (L_i^{(r)}(t) - L_{i,0}^{(r)})$ to avoid numerical artefacts at big cell deformation. These two definitions are the same for small cell deformations. Time is discretized in time steps $dt = 0.01$ min and the parameter ξ order of magnitude is tuned to observe the dynamics of the system evolution on the minute/hour timescale. Our previous equilibrium model predicts that matching will occur when $K \sim T_{adh}$ and on the hour timescale when $T_{adh}/\xi \sim 1 \mu m / min$. In Figure 6, T_{adh} and K are expressed in pN and ξ in pN * min / μm . The vertices positions are calculated at each simulation step and allow to calculate the mismatch evolution in time.

References

1. Lecuit, T. & Le Goff, L. Orchestrating size and shape during morphogenesis. *Nature* 450, 189–192 (2007).
2. Heisenberg, C.-P. & Bellaiche, Y. Forces in Tissue Morphogenesis and Patterning. *Cell* 153, 948–962 (2013).
3. Collinet, C., Rauzi, M., Lenne, P.-F. & Lecuit, T. Local and tissue-scale forces drive oriented junction growth during tissue extension. *Nat. Cell Biol.* 17, 1247–1258 (2015).
4. Pinheiro, D. & Bellaiche, Y. Mechanical Force-Driven Adherens Junction Remodeling and Epithelial Dynamics. *Dev. Cell* 47, 3–19 (2018).
5. Olivotto, I., Cecchi, F., Poggesi, C. & Yacoub, M. H. Developmental origins of hypertrophic cardiomyopathy phenotypes: a unifying hypothesis. *Nat. Rev. Cardiology* 6, 317–321 (2009).
6. Som, P. M. & Naidich, T. P. Illustrated Review of the Embryology and Development of the Facial Region, Part 1: Early Face and Lateral Nasal Cavities. *AJNR Am. J. Neuroradiol.* 34, 2233–2240 (2013).
7. Dixon, M. J., Marazita, M. L., Beaty, T. H. & Murray, J. C. Cleft lip and palate: understanding genetic and environmental influences. *Nature* 12, 167–178 (2011).
8. Clandinin, T. R. & Zipursky, S. L. Making connections in the fly visual system. *Neuron* 35, 827–841 (2002).
9. Sanes, J. R. & Yamagata, M. Many Paths to Synaptic Specificity. *Annu. Rev. Cell Dev. Biol.* 25, 161–195 (2009).
10. Pinto-Teixeira, F. et al. Development of Concurrent Retinotopic Maps in the Fly Motion Detection Circuit. *Cell* 173, 485–498.e11 (2018).
11. Takeichi, M. The cadherin superfamily in neuronal connections and interactions. *Nat. Rev. Neurosci.* 8, 11–20 (2006).
12. Hong, W., Mosca, T. J. & Luo, L. Teneurins instruct synaptic partner matching in an olfactory map. *Nature* 484, 201–207 (2012).
13. Maness, P. F. & Schachner, M. Neural recognition molecules of the immunoglobulin superfamily: signaling transducers of axon guidance and neuronal migration. *Nat. Neurosci.* 10, 19–26 (2007).
14. Berns, D. S., DeNardo, L. A., Pederick, D. T. & Luo, L. Teneurin-3 controls topographic circuit assembly in the hippocampus. *Nature* 554, 328–333 (2018).
15. Harada, T., Harada, C. & Parada, L. F. Molecular regulation of visual system development: more than meets the eye. *Genes & Development* 21, 367–378 (2007).
16. Kumar, J. P. Building an ommatidium one cell at a time. *Dev. Dyn.* 241, 136–149 (2011).
17. Wartlick, O., Julicher, F. & Gonzalez-Gaitan, M. Growth control by a moving morphogen gradient during *Drosophila* eye development. *Development* 141, 1884–1893 (2014).
18. Olson, E. N. Gene Regulatory Networks in the Evolution and Development of the Heart. *Science* 313, 1922–1927 (2006).
19. Hunter, G. L. et al. Coordinated control of Notch/Delta signalling and cell cycle progression drives lateral inhibition-mediated tissue patterning. *Development* 143, 2305–2310 (2016).
20. Shaya, O. et al. Cell-Cell Contact Area Affects Notch Signaling and Notch-Dependent Patterning. *Dev. Cell* 40, 505–511.e6 (2017).
21. Gibson, M. C., Patel, A. B., Nagpal, R. & Perrimon, N. The emergence of geometric order in proliferating metazoan epithelia. *Nature* 442, 1038–1041 (2006).

22. Umetsu, D. et al. Local increases in mechanical tension shape compartment boundaries by biasing cell intercalations. *Curr. Biol.* 24, 1798–1805 (2014).
23. Hamant, O. et al. Developmental patterning by mechanical signals in *Arabidopsis*. *Science* 322, 1650–1655 (2008).
24. Taniguchi, K. et al. Chirality in planar cell shape contributes to left-right asymmetric epithelial morphogenesis. *Science* 333, 339–341 (2011).
25. Hervieux, N. et al. A Mechanical Feedback Restricts Sepal Growth and Shape in *Arabidopsis*. *Curr. Biol.* 26, 1–10 (2016).
26. Le Garrec, J.-F. et al. A predictive model of asymmetric morphogenesis from 3D reconstructions of mouse heart looping dynamics. *eLife* 6, 421 (2017).
27. Matejčić, M., Salbreux, G. & Norden, C. A non-cell-autonomous actin redistribution enables isotropic retinal growth. *PLoS Biol.* 16, e2006018–29 (2018).
28. Collier, J. R., Monk, N. A., Maini, P. K. & Lewis, J. H. Pattern formation by lateral inhibition with feedback: a mathematical model of delta-notch intercellular signalling. *J. Theor. Biol.* 183, 429–446 (1996).
29. Kim, S., Cassidy, J. J., Yang, B., Carthew, R. W. & Hilgenfeldt, S. Hexagonal Patterning of the Insect Compound Eye: Facet Area Variation, Defects, and Disorder. *Biophys. J.* 111, 2735–2746 (2016).
30. Bi, D., Lopez, J. H., Schwarz, J. M. & Manning, M. L. A density-independent rigidity transition in biological tissues. *Nature Physics* 11, 1074–1079 (2015).
31. Hayashi, T. & Carthew, R. W. Surface mechanics mediate pattern formation in the developing retina. *Nature* 431, 647–652 (2004).
32. Zhang, S., Amourda, C., Garfield, D. & Saunders, T. E. Selective Filopodia Adhesion Ensures Robust Cell Matching in the *Drosophila* Heart. *Dev. Cell* 46, 189–203.e4 (2018).
33. Bodmer, R., Heart, M. F. 2010. Heart Development and Regeneration: Development and Aging of the *Drosophila* Heart. 47–84 (Academic Press, 2010).
34. Kuntz, S. G. & Eisen, M. B. *Drosophila* Embryogenesis Scales Uniformly across Temperature in Developmentally Diverse Species. *PLoS Genet.* 10, e1004293 (2014).
35. Chong, J., Amourda, C. & Saunders, T. E. Temporal development of *Drosophila* embryos is highly robust across a wide temperature range. *J. R. Soc. Interface* 15, 20180304–11 (2018).
36. Atia, L. et al. Geometric constraints during epithelial jamming. *Nature Physics* 14, 613–620 (2018).
37. Bentley, K., Mariggi, G., Gerhardt, H. & Bates, P. A. Tipping the Balance: Robustness of Tip Cell Selection, Migration and Fusion in Angiogenesis. *PLoS Comput. Biol.* 5, e1000549–19 (2009).
38. Sonnemann, K. J. & Bement, W. M. Wound Repair: Toward Understanding and Integration of Single-Cell and Multicellular Wound Responses. *Annu. Rev. Cell Dev. Biol.* 27, 237–263 (2011).
39. Koser, D. E. et al. Mechanosensing is critical for axon growth in the developing brain. *Nat. Neurosci.* 19, 1592–1598 (2016).
40. Barriga, E. H., Franze, K., Charras, G. & Mayor, R. Tissue stiffening coordinates morphogenesis by triggering collective cell migration in vivo. *Nature* 554, 523–527 (2018).
41. Krauth, W. Statistical mechanics: algorithms and computations. (Oxford University Press, 2006).
42. Metropolis, N., Rosenbluth, A. W., Rosenbluth, M. N., Teller, A. H. & Teller, E. Equation of State Calculations by Fast Computing Machines. *J. Chem. Phys.* 21, 1087–1092 (1953).